

KIC 8975515: a fast-rotating (γ Dor - δ Sct) hybrid star with Rossby modes and a slower δ Sct companion in a long-period orbit

A. Samadi-Ghadim^{1,2}, P. Lampens³, D. M. Jassur⁴, and P. Jofré¹

¹ Núcleo de Astronomía, Facultad de Ingeniería y Ciencias, Universidad Diego Portales, Av. Ejército Libertador 441, Santiago, Chile
e-mail: anya.samadi@mail_udp.cl

² Research Institute for Applied Physics and Astronomy, University of Tabriz, P.O.Box 51664, Tabriz, Iran

³ Koninklijke Sterrenwacht van België, Ringlaan 3, B-1180 Brussel, Belgium

⁴ Department of theoretical Physics and Astrophysics, Physics Faculty, University of Tabriz, P.O. Box 51664, Tabriz, Iran

April 8, 2020; submitted

ABSTRACT

Aims. KIC 8975515 is a *Kepler* double-lined spectroscopic binary system with hybrid pulsations. Two components have similar atmospheric properties ($T_{\text{eff}} \sim 7400$ K), and one of them is a fast rotator ($v \sin i = 162$ versus 32 km/s). Our aim is to study the *Kepler* light curve in great detail in order to determine the frequencies of the pulsations, to search for regular spacing patterns in the Fourier spectrum, if any, and to discuss their origin in the context of binarity and fast rotation.

Methods. In this paper, we study the properties of the stellar pulsations based on a careful analysis in the low-, intermediate- and high-frequency regions of the Fourier spectrum. This is done by performing repeated frequency-search analyses with successive prewhitenings of all the significant frequencies detected in the spectrum. Moreover, we searched for regular period spacings among the g modes, as well as frequency splitting among the g and p modes.

Results. In the low-frequency regime, five regular period spacing patterns including one series of prograde g modes and four series of retrograde r modes were detected. The r modes are well-distributed with respect to the harmonics of the rotational frequency of the fast-rotating star $f_{\text{rot}} = 1.647$ d $^{-1}$. The dominant g mode is $f_2 = 2.37$ d $^{-1}$. The strongest p mode, at $f_1 = 13.97$ d $^{-1}$, forms a singlet. In the high-frequency region, we identified two multiplets of regularly split p modes with mean frequency spacings of 0.42 d $^{-1}$ and 1.65 d $^{-1}$.

Conclusions. We detected some series of retrograde r and prograde g modes as well as two multiplets of p modes with frequency spacings related to the stellar rotation of both components of the twin system KIC 8975515. We identified the fast-rotating component as a hybrid pulsator with r modes and the slowly-rotating component as a δ Scuti pulsator.

Key words. Techniques: photometric (Fourier) - Techniques: spectroscopic - (Stars:) binaries: spectroscopic - Stars: variables: δ Scuti - Stars: variables: γ Dor - Asteroseismology

1. Introduction

Asteroseismology is a formidable tool in astrophysics, which allows us to investigate the interior structure of stars based on phenomena observed at their surface. This knowledge is essential for a detailed understanding of both stellar structure and stellar evolution. γ Dor/ δ Scuti variables, two subgroups of classical A/F-type pulsators, are intriguing objects with regard to their stellar interior. They are located at the cross-section of the Cepheid instability strip and the main sequence. The first subgroup comprises the γ Dor variables of spectral type A7-F5. They have masses, M , from 1.5 to 1.8 M_{\odot} and temperatures, T_{eff} , from 6700 to 7400 K (Catelan & Smith 2015). Their pulsations are mainly due to low-degree ($\ell \ll 4$) high-radial order ($20 \lesssim n \lesssim 120$) gravity (g) modes (Van Reeth et al. 2016; Saio et al. 2018) which occur in the radiative zones close to the stellar core. The fact that these modes are excited in the deep stellar interior provides us with important information about the chemical gradient of the different layers. As a result of the excited high-radial order g modes (Shibahashi 1979; Tassoul 1980), the occurrence of deviations from a uniform period spacing reveals the chemical inhomogeneities of the near-core convective structures (Miglio et al. 2008). The typical period of their pulsation modes lies in the range from 0.3 to 3 days. Studying the

pulsations of γ Dor stars with intermediate to fast rotation provides information on their differential rotation, the angular momentum transport between the layers (e.g. Ouazzani et al. 2017; Li et al. 2019a,b) and other physical processes from the different excitation layers.

Van Reeth et al. (2016) detected the first observational evidence of r modes (global Rossby waves) - alongside g modes - for γ Dor stars with significant rotation. Recently, Li et al. (2019b) reported the detection of both r and g mode period spacing patterns for 82 γ Dor stars. In the absence of considerable stellar rotation, toroidal motions associated to r modes cannot provide any compression nor expansion. Hence, the stellar atmospheres undergo neither any restoring force nor any light variations. However, in the rapidly rotating regime the toroidal motions get coupled with spheroidal motions and they present themselves as temperature perturbations. Furthermore, coupling of spheroidal motions provides excitation of the r modes by the κ mechanism (e.g. DA white dwarfs in Saio 1982; Berthomieu & Provost 1983). r modes appear at lower frequencies than the (prograde) g mode frequencies and their period spacings form a retrograde pattern (Van Reeth et al. 2016; Saio et al. 2018; Li et al. 2019b). Saio et al. (2018) showed that r modes of azimuthal order m appear at frequencies lower than m times the rotational frequency.

The second subgroup, the δ Scuti variables are intermediate-mass, pre-main sequence (Zwintz et al. 2014), main sequence (Aerts et al. 2010) or post-main sequence (Breger 2007) stars in the classical instability strip. They are slightly hotter than γ Dor stars with masses, M , from 1.5 to $2.5 M_{\odot}$ and temperatures, T_{eff} , from 6900 to 8900 K. Their pulsation periods range from 0.01 d to 0.25 d (15 min to 6 hr) (Aerts et al. 2010; Catelan & Smith 2015). This group pulsates in radial and non-radial, low-degree ($\ell = 1 - 3$) and low-overtone ($n = 0, 1, 2, 3, \dots$) p modes (Aerts et al. 2010; Sánchez Arias et al. 2017). The p modes are excited near the surface and reflect the physical properties of the stellar envelope.

Based on theoretical computations, Xiong et al. (2016) showed that the δ Scuti and the γ Dor pulsators may describe a single, larger instability strip. In the region where both theoretical instability strips overlap, we expect to find hybrid behaviour (Balona & Dziembowski 2011; Xiong et al. 2016). This is clearly seen in the observational colour-magnitude diagrams, *e.g.* from *Kepler* (Bradley et al. 2015). Hybrid stars must have both detectable g modes (in the low(er)-frequency range) and detectable p modes (in the high(er)-frequency range) in their Fourier spectrum.

The mode driving mechanism(s) for hybrid stars (γ Dor/ δ Sct or δ Sct/ γ Dor) is (are) not well-understood. For all the classical pulsators located in the Cepheid instability strip, *e.g.* the δ Scuti stars, the κ mechanism is believed to be the major excitation mechanism (Handler 1999; Houdek et al. 1999; Balona et al. 2015). Furthermore, turbulent pressure may also contribute in driving p modes in δ Sct stars (Houdek 2000; Antoci et al. 2014). Whereas, for γ Dor stars, convective flux blocking (at the bottom of the convection zone) is thought to drive the pulsations (Guzik et al. 2000; Dupret et al. 2004, 2005). The study by Xiong et al. (2016), shows that for the hot δ Scuti and γ Dor stars, the (radiative) κ mechanism is the main driving force for both p and g modes, whereas, for the cool δ Sct/ γ Dor stars, it is the coupling of convection and oscillations which excites or damps the pulsations. The much larger instability strip described by Xiong et al. (2016) extends well beyond the borders of the classical instability strips of the γ Dor and the δ Sct stars, respectively (*e.g.* Handler 1999; McNamara 2000; Dupret et al. 2004). Indeed, from an observational perspective, the width of the δ Scuti instability strip was shown to extend beyond the theoretical edges (Bowman & Kurtz 2018). Murphy et al. (2019) derived a new empirical instability strip that is much wider (and somewhat hotter) than the theoretical ones (*e.g.* Handler 1999). The detection of pulsations in binary systems not only provides an additional tool to derive stellar parameters in an independent way but is also the perfect laboratory to check the influence of binarity (*e.g.* eccentricity, tidal effects (Samadi-Ghadim et al. 2018a; Guo et al. 2017), mass transfer (Mkrtichian et al. 2018), chemical peculiarities (Kolbas et al. 2012), presence of a third body (Samadi-Ghadim et al. 2010; Gies et al. 2015), etc.) on stellar structure, stellar evolution and the excited oscillation modes. Based on various surveys, the fraction of multiple systems in a population, MF, among the intermediate-mass stars is $MF_{1.5-5M_{\odot}}^{MS} \geq 50\%$ (Duchêne & Kraus 2013). Moreover, the observed frequency of spectroscopic binaries among field intermediate-mass stars is in the range of 30–45% (Duchêne & Kraus 2013). Thus, we may expect that a significant fraction of the γ Dor/ δ Scuti stars resides in binary or multiple systems. Eventually, more than 2200 *Kepler* main-sequence A/F-type stars were studied using the pulsation timing method in search of binarity across a narrow interval in (log) period allowed by the method (Murphy et al. 2018). These authors de-

tected a binary fraction of $13.9 \pm 2.1\%$ among the studied sample. In comparison, Lampens et al. (2018) reported an extensive multi-epoch spectroscopic survey of 50 *Kepler* hybrid pulsators for which they derived a multiplicity fraction of at least 27%.

Stellar pulsation studies exploiting ever more precise photometric data from space missions such as *CoRoT* (Baglin et al. 2006), *Kepler* (Koch et al. 2010) (*K2*), *TESS* (Ricker et al. 2015) have become very fruitful as these missions provide light curves of unprecedented accuracy with errors of the order of few μmag (*i.e.* few parts per million). These space missions allowed the detection of several hundreds of hybrid γ Dor/ δ Sct pulsators exhibiting both types of modes simultaneously, be it with very low amplitudes. For a detailed historical review of the discoveries, we refer to Qian et al. (2019). We briefly review a few extensive studies concerning systems with hybrid pulsations here. Examples of such studies are: KIC 4544587, an eccentric eclipsing binary system with an orbital period $P_{\text{orb}} = 2.19$ days (Hambleton et al. 2013); KIC 10080943, a double-lined spectroscopic binary with $P_{\text{orb}} = 15.34$ days (Schmid et al. 2015; Keen et al. 2015); KIC 9592855, a post-mass-transfer eclipsing binary with $P_{\text{orb}} = 1.2$ days (Guo et al. 2017); KIC 4150611, a quintuplet system where the primary is a triplet (Hełminiak et al. 2017) and KIC 6048106, an Algol-type eclipsing binary with $P_{\text{orb}} = 1.56$ days (Lee 2016; Samadi-Ghadim et al. 2018b,a). In addition, Derekas et al. (2019) discovered the double-lined spectroscopic binary KIC 5709664 (using the phase modulation (PM) method (Murphy et al. 2014) and fitting of radial velocity data) with both r - and p -modes.

In this paper, we focus our attention on a *Kepler* (candidate) hybrid pulsating star recently discovered as a double-lined, long-period, high mass-ratio, spectroscopic binary system (SB2), KIC 8975515. Our goal is to detect the pulsation frequencies and to characterise the pulsations using the photometric *Kepler* data. The properties of the *Kepler* light curves are described in Sec. 2. We describe our methodology for the pulsation study in Sec. 3. The details and results of the frequency analyses for both the high- and the low-frequency regions are presented in Sec. 4. We discuss all the results brought together in Sec. 5. Finally, in Sec. 6, we present a summary and our main conclusions.

2. Photometric observations from the *Kepler* mission

KIC 8975515, a bright *Kepler* object with $K_p = 9.515$ mag, was observed during the quarters Q0–Q17 in Long Cadence mode (LC with a sampling of 29.42 min). There are four months of observations in Short Cadence (SC) mode available with a sampling of 58.85 s from the quarters Q2.3, Q5.1, Q5.2 and Q5.3. Altogether, we have 1470.46 days ($f_{\text{res}} = 0.00068 \text{ d}^{-1}$)¹ of LC and 121.79 d of SC ($f_{\text{res}} = 0.00821 \text{ d}^{-1}$) data available. For the light curves, we took the *Kepler* original flux and its error for all quarters from the Kepler Asteroseismic Science Operations Centre (KASOC). We first converted the flux to magnitude and then applied a polynomial fit to each quarter. The fit was then subtracted from the original data in order to smooth the trends in each quarter. We finally concatenated the light curves of all quarters and removed the outliers manually. The ‘detrended’ light curve in LC mode was used for this pulsation study.

A close-up view of the light variations of KIC 8975515 is shown in Fig. 1 for both LC and SC sampling modes. The relative magnitude varies with a semi-amplitude of 1 mmag on average.

KIC 8975515 was first studied and reported as an A/F-type

¹ The frequency resolution equals (time span of the observations)⁻¹

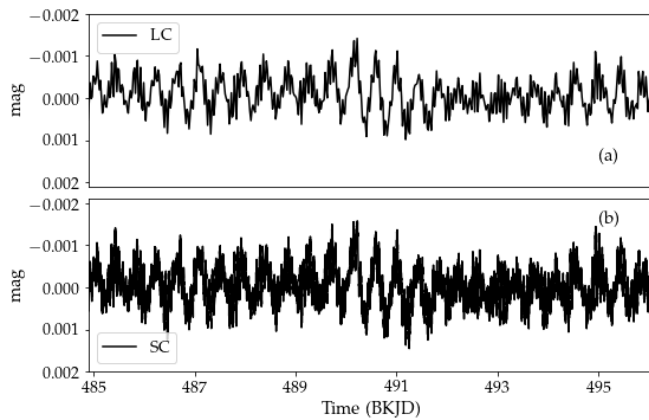


Fig. 1. Close-up view of the light variations of KIC 8975515. The vertical axis displays the relative magnitude (mag) while the horizontal axis displays the Barycentric *Kepler* Julian Date (BKJD = BJD - 2454833.0) in days. (a) An 11-day interval of the Long-Cadence (LC) light curve from Q6. (b) The same time interval of the Short-Cadence (SC) light curve.

hybrid star by Uytterhoeven et al. (2011). We list the information available from *Kepler* Input Catalogue in Table 1 (derived with the assumption of single star). Moreover, *Gaia* DR2 (Gaia Collaboration et al. 2018a,b) measured a parallax of $\varpi = 2.506 \pm 0.0387$ mas for this target. The projected rotational velocities are those from Lampens et al. (2018). The orbital parameters such as P_{orb} , the eccentricity, e , and the mass ratio, q , (the ratio of $a_1 \sin i$ (Table 11) and $a_2 \sin i$ (Table 8) reported by Lampens et al. (2018) shows that $q \sim 0.8$) indicate that the system consists of two stars of almost similar mass in a long-period, eccentric orbit. The updated values in Table 1 are from Lampens et al. (priv. comm.).

3. Methodology of the pulsation study

Our approach is based on the Lomb-Scargle periodogram (Lomb 1976; Scargle 1982). We calculated the periodogram of the observed light curves up to the Nyquist frequency (both LC and SC samplings with $f_{\text{NyLC}} = 24.65 \text{ d}^{-1}$ and $f_{\text{NySC}} = 734.07 \text{ d}^{-1}$). The Signal-to-Noise Ratio (SNR) of each frequency was calculated in a box-size of 2 d^{-1} . The prewhitening method is from Vaniček (1971). We consider a frequency significant only if $\text{SNR} \geq 4$, based on Breger et al. (1993)'s criterion. For detailed information on the frequency analysis and the prewhitening methods, along with the error determination see Samadi-Ghadim et al. (2018a). We consider two frequencies as resolved if their difference is larger than the resolution frequency, $f_{\text{res}} = 1/T$, which is 0.00068 d^{-1} for the LC light curve. This procedure provided us with a list of prewhitened frequencies of acceptable SNR and amplitude. We will refer to them as 'significant' frequencies and we will check the possible origin (whether they can be due to pulsations or caused by some other mechanism). During the frequency analysis we also checked whether any significant frequency is a linear combination of the previous frequencies of the highest SNR and larger amplitudes (i.e. having larger than mean SNR and mean amplitude of the previously prewhitened g modes).

According to asymptotic theory of stellar pulsations (Shibahashi 1979; Tassoul 1980) regular period spacing may occur for the high-radial order g modes, $n \gg l$, with n and l the radial order and the degree of the mode, respectively. In contrast, for the p modes, regular splitting may occur because of the rotation. For

Table 1. Information on KIC 8975515 from surveys and data bases.

Survey	Target ID	
<i>Kepler</i>	KIC 8975515	
2MASS	J19534557+4513092	
TYC	3558-2169-1	
Gaia	2079403021883452288	
KIC ⁽¹⁾		
Parameter	Value	
RA	+19 ^h :53 ^m :45.5766 ^s	
Dec	+45°:13':9.274"	
LC	Q0-Q17	
SC	Q2.3, Q5.1, 5.2, 5.3	
BJD ₀ (LC)(d)	2454953.5385	
Kmag (mag)	9.515	
T _{eff} (K)	7176	
log g (cgs)	3.896	
R (R_{\odot})	2.197	
GAIA DR2 ⁽²⁾		
ϖ (mas)	2.506 ± 0.0387	
$m_G^{(3)}$ (mag)	9.447	
T _{eff} (K)	7157	
Spectroscopy ⁽⁴⁾		
Parameter	Primary	Secondary
$v \sin i$ (km/s)	162±2	32±1
T _{eff} (K)	$7440 \pm 250^{(5)}$	7380 ± 250
Parameter	Value ⁽⁶⁾	Uncertainty
P_{orb} (d)	1603	9
e	0.408	0.015
q	0.83	0.05

References. (1) from Kepler Input Catalogue (based on 5-band photometry (plus the J, H, & K bands from the 2MASS survey) considering that the object is a single star); (2) Gaia Collaboration et al. (2018a,b); (3) mean G-band magnitude; (4) Lampens et al. (2018); (5) The uncertainty was estimated from a partial comparison of effective temperatures measured with those from the literature (Lampens et al. 2018, Fig. 7); (6) Lampens et al. (2020) *in prep.* (priv. communic.)

genuine hybrid stars, we can expect to see these regularities in the period and frequency domains for the g modes and in the frequency domain for the p modes. The regular period spacings, for the g and p modes, can be affected by rotation or chemical inhomogeneities (Bouabid et al. 2013; Li et al. 2019b).

4. Frequency analysis

Fig.2 shows the Fourier spectrum both for the LC and SC *Kepler* light curves. The full Fourier spectrum is shown in pink while the significant frequencies are presented in black. In the case of SC observations, the illustration (panel (b) in Fig. 2) shows a close-up view of the frequency range (0-25 d^{-1}) where some significant frequencies show up. Clearly, both LC and SC frequency spectra present almost the same features. For the current study we used the LC light curve with the longest time base. The list of detected significant frequencies is presented in Table A2. It is sorted according to decreasing amplitude. In total we re-

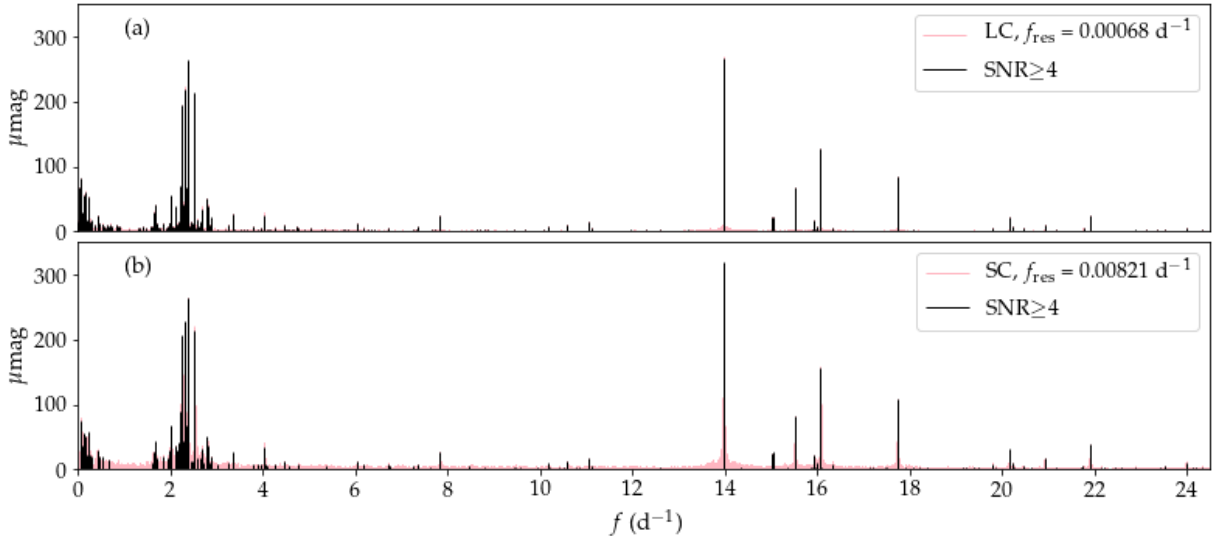


Fig. 2. Fourier Spectrum of KIC 8975515 (pink). (a) Frequency spectrum associated to LC observations (pink) and the significant frequencies with $\text{SNR} \geq 4.0$ in a box size of $2d^{-1}$ (black). (b) Same as (a) but for the SC observations (referring to the quarters Q2.3 and Q5.1, 5.2, 5.3). There is no significant frequency between 25 and $50 d^{-1}$ and we clipped it off from the illustration.

solved 331 frequencies.

Interestingly, we can see that the dominant modes pertain to both the low and the high-frequency regions. Indeed, the dominant frequency in the high-frequency region, $f_1 = 13.97236 \pm 0.00001 d^{-1}$, has an amplitude of $A_1 = 268 \pm 5 \mu\text{mag}$, while the most significant frequency in the g mode region, $f_2 = 2.37418 \pm 0.00001 d^{-1}$, occurs with very similar amplitude, $A_2 = 265 \pm 5 \mu\text{mag}$.

Next we searched for the frequencies that are combinations of the most significant frequencies, *i.e.* 'parent' frequencies. The parent frequencies were chosen among low-frequency modes up to $3.3 d^{-1}$ and have both amplitude and SNR higher than the corresponding mean values (*i.e.* $A_{\text{mean}} = 13 \mu\text{mag}$ and $\text{SNR}_{\text{mean}} = 14.9$) of the detected frequencies. Accordingly, we selected 24 frequencies as parent frequencies. Furthermore, we searched for the combination of $13.97 d^{-1}$ with any low-frequency mode to reveal the high frequencies which might appear as coupling of f_1 and g modes. This can help to detect low- and high-frequency modes originating from the same star. Generally, a combination frequency will have its amplitude smaller than that of both parent frequencies and the difference between this linear combination (of the parent frequencies) and the candidate combination frequency should match within a tolerance of the resolution frequency (*e.g.* Zhang et al. 2018). The results are reported in Table A2 and we indicate the parent frequencies with a check-mark under the column 'P'. The subscript '*' means that the detected frequency is not a unique combination of parent frequencies. Moreover, the frequencies that are a possible harmonic of any parent frequency are also reported in Table A2.

4.1. The high-frequency region

A quick look at Fig. 2 and a close-up view of the high-frequency section of Fig 3 (b) shows that the p modes are very sparsely distributed and extend to $22 d^{-1}$, unlike the distribution of the g modes (4.2). The significant frequencies have amplitudes ranging from $A = 1$ to $268 \mu\text{mag}$.

Because of non-linear effects, the combination of the g modes, f_g , and the dominant p mode ($f_{p_{\text{max}}}$) may generate some coupled

frequency peaks in the form of $f_{p_{\text{max}}} \pm f_g$ (Kurtz et al. 2014). We found f_{303} ($11.96 d^{-1}$) to be a combination of f_1 and f_{16} ($2.79 d^{-1}$) that is a prograde g mode. On the other hand f_{285} ($12.29 d^{-1}$) is a combination of f_1 and f_{18} which is a retrograde mode. Similarly f_{94} ($10.59 d^{-1}$) is a combination of f_1 with another retrograde mode (f_{35}). We refer to these frequencies with 'MC' in Table A2. We ran a Monte Carlo simulation and found that each combination has about 2% probability of occurring by random chance.

We detected two different types of multiplets: doublets and triplets with the (semi-)regular frequency spacing of $\Delta f_{\text{mean}_1} = 0.419 \pm 0.020 d^{-1}$ (magenta in Fig. 3) and $\Delta f_{\text{mean}_2} = 1.654 \pm 0.018 d^{-1}$ (blue in Fig. 3), located on either side of f_1 , though not involving f_1 . The quoted error is the standard deviation. Table 2 lists the associated frequencies in d^{-1} and the Δf value between each couple of them where $\epsilon_{\Delta f}$ equals $\sqrt{\epsilon_{f_1}^2 + \epsilon_{f_2}^2}$. Fig. 3, presents the associated frequencies (lower panel) and their Δf values (upper panel) distinguishable by two different colours and symbols, respectively. We detected one frequency in the g mode region f_{200} ($1.6467 \pm 0.0001 d^{-1}$) which is equal to the larger frequency splitting within the errors ($1.654 \pm 0.018 d^{-1}$). However, there are other groups of frequencies in the interval (6.72 to $8.63 d^{-1}$) that are either a combination of prograde g modes (f_{156}, f_{262}) or a combination of prograde g and retrograde r modes (f_{145}, f_{28} and f_{281}). We suggest that the larger frequency splitting is related to the fast rotating companion and the smaller is related to the slowly rotating one. We will present arguments in favor in Sec. 5.

We present the échelle diagram (Fig. 4) for all the significant high frequencies, using the large mean frequency splitting from Table 2. Panel (a) in Fig. 4 shows the frequency modulo the mean frequency splitting associated to the slowly rotating star $f_{\text{rot}} = 0.419 d^{-1}$. The symbol size is associated to the mode amplitudes and the colour coding is similar to Fig. 3. We highlighted these frequencies using magenta circles. Similarly in panel (b) we show the modes with detected regular splittings versus modulo $f_{\text{rot}} = 1.654 d^{-1}$ which we associated to the fast rotating star. We highlighted the modes with this average

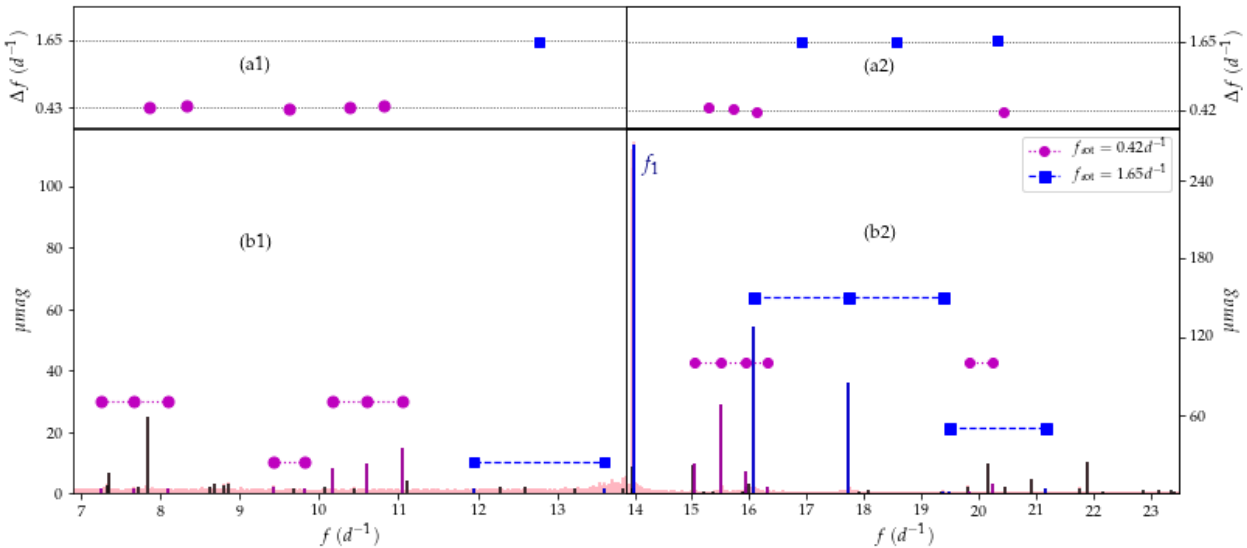


Fig. 3. Regular frequency spacing for p modes. (a1,a2) Frequency splittings and their deviation from mean frequency splitting (Table 2). (b1,b2) Associated frequencies of the detected multiplets of significant frequencies (black) and the full frequency spectrum (pink).

Table 2. p modes with (quasi-)regular frequency splitting in the Fourier spectrum of KIC 8975515 (Fig. 3). SR/FR: detected p modes are most probably associated to Slowly Rotating/Fast Rotating star. $\epsilon_{\Delta f}$ is $\sqrt{\epsilon_{f_1}^2 + \epsilon_{f_2}^2}$. σ_{Δ} is the standard deviation.

f_i	$f \pm \epsilon_f$ d^{-1}	A μmag	Π d	$\Delta f \pm \epsilon_{\Delta f}$ d^{-1}	SNR	color	comment
						Fig. 3 (b)	
f_{301}	7.24786 ± 0.00026	1.63	0.13797		6	●	SR
f_{299}	7.65563 ± 0.00026	1.75	0.13062	0.4078 ± 0.0004	7	●	SR
f_{304}	8.10046 ± 0.00027	1.56	0.12345	0.4448 ± 0.0004	6	●	SR
f_{278}	9.42582 ± 0.00029	2.23	0.10609		11	●	SR
f_{308}	9.81926 ± 0.00030	1.51	0.10184	0.3934 ± 0.0004	7	●	SR
f_{116}	10.16604 ± 0.00015	8.08	0.09837		31	●	SR
f_{94}	10.59499 ± 0.00013	9.72	0.09438	0.4289 ± 0.0002	30	●	SR
f_{51}	11.04825 ± 0.00009	14.65	0.09051	0.4532 ± 0.0001	30	●	SR
f_{32}	15.05250 ± 0.00006	22.82	0.06643		30	●	SR
f_9	15.51470 ± 0.00003	68.71	0.06446	$0.4621(9) \pm 0.00006$	77	●	SR
f_{45}	15.94343 ± 0.00008	16.27	0.06272	$0.4287(3) \pm 0.00009$	30	●	SR
f_{193}	16.32732 ± 0.00022	5.00	0.06125	0.3839 ± 0.0002	27	●	SR
f_{326}	19.35654 ± 0.00036	1.16	0.05166		6	●	SR
f_{184}	19.80269 ± 0.00022	5.28	0.05050	0.4461 ± 0.0004	31	●	SR
f_{127}	20.23788 ± 0.00017	7.31	0.04941	0.4352 ± 0.0003	30	●	SR
						$\Delta f_{\text{mean}} \pm \sigma_{\Delta}$	0.419 ± 0.020
f_{303}	11.95624 ± 0.00030	1.60	0.08364		7	■	FR
f_{320}	13.58882 ± 0.00036	1.27	0.07359	1.6326 ± 0.0005	7	■	FR
f_6	16.07633 ± 0.00002	128.14	0.06220		76	■	FR
f_7	17.73452 ± 0.00002	84.42	0.05639	$1.6581(9) \pm 0.00003$	77	■	FR
f_{305}	19.38475 ± 0.00039	1.55	0.05159	1.6502 ± 0.0004	9	■	FR
f_{311}	19.48475 ± 0.00037	1.42	0.05132		8	■	FR
f_{249}	21.16071 ± 0.00027	3.00	0.04726	1.6759 ± 0.0005	19	■	FR
						$\Delta f_{\text{mean}} \pm \sigma_{\Delta}$	1.654 ± 0.018

splitting using blue squares.

4.2. The low-frequency region

We carefully investigated the period spectrum in search of any regular period spacing pattern. The upper panel in Fig. 5 shows different patterns of period spacing $\Delta\Pi$ that are either prograde (blue squares) or retrograde (green triangles and cyan circles). Their associated periods and frequencies with similar colours

Table 3. Detected g modes in the Fourier spectrum of KIC 8975515 (Long Cadence observations). *FR* suggests that the suggested origin of the modes is the fast-rotating star ($v \sin i = 162$ km/s).

f_i	$f \pm \epsilon_f$ d^{-1}	A μmag	Π d	$\Delta\Pi \pm \epsilon_{\Delta\Pi}$ s	SNR	colour Fig. 5	comment
f_{37}	2.89346 ± 0.00006	20.83	0.34561		31	■	FR; $m = -2?$
f_{83}	2.83861 ± 0.00008	9.61	0.35229	577 ± 312	15	■	FR; $m = -2?$
f_{95}	2.78938 ± 0.00003	51.37	0.35850	537 ± 272	30	■	FR; $m = -2?$
f_{54}	2.63465 ± 0.00006	14.21	0.37956		19	■	FR; $m = -2?$
f_{147}	2.60372 ± 0.00009	6.69	0.38407	390 ± 124	10	■	FR; $m = -2?$
f_{40}	2.57491 ± 0.00005	16.79	0.38836	371 ± 106	22	■	FR; $m = -2?$
f_{157}	2.54831 ± 0.00010	6.18	0.39242	350 ± 85	9	■	FR; $m = -2?$
f_4	2.52345 ± 0.00001	213.96	0.39628	334 ± 69	70	■	FR; $m = -2?$
f_{72}	2.47839 ± 0.00007	11.37	0.40349		13	■	FR; $m = -2?$
f_{49}	2.45825 ± 0.00005	14.90	0.40679	286 ± 22	15	■	FR; $m = -2?$
f_{146}	2.43813 ± 0.00009	6.69	0.41015	290 ± 26	9	■	FR; $m = -2?$
f_{152}	2.42171 ± 0.00009	6.43	0.41293	240 ± 24	9	■	FR; $m = -2?$
f_{143}	2.40690 ± 0.00009	6.77	0.41547	220 ± 44	9	■	FR; $m = -2?$
f_{182}	2.38873 ± 0.00010	5.34	0.41863		8	■	FR; $m = -2?$
f_2	2.37418 ± 0.00001	264.99	0.42120	222 ± 44	77	■	FR; $m = -2?$
f_{140}	2.32178 ± 0.00008	6.93	0.43070		9	■	FR; $m = -2?$
f_3	2.31022 ± 0.00001	219.12	0.43286	186 ± 79	79	■	FR; $m = -2?$
f_{129}	2.29919 ± 0.00008	7.23	0.43494	179 ± 86	9	■	FR; $m = -2?$
f_{17}	2.28902 ± 0.00003	41.86	0.43687	167 ± 98	31	■	FR; $m = -2?$
f_{219}	2.27908 ± 0.00010	4.30	0.43877	164 ± 101	6	■	FR; $m = -2?$
f_{25}	2.26457 ± 0.00004	28.55	0.44158		27	■	FR; $m = -2?$
f_5	2.25761 ± 0.00001	194.15	0.44295	118 ± 147	80	■	FR; $m = -2?$
f_{50}	2.23396 ± 0.00005	14.84	0.44763		15	■	FR; $m = -2?$
f_8	2.22490 ± 0.00002	70.43	0.44946	157 ± 108	30	■	FR; $m = -2?$
f_{11}	2.21884 ± 0.00002	65.65	0.45069		30	■	FR; $m = -2?$
f_{107}	2.21165 ± 0.00007	8.82	0.45215	127 ± 137	11	■	FR; $m = -2?$
f_{31}	2.19728 ± 0.00004	23.44	0.45511		22	■	FR; $m = -2?$
f_{109}	2.19179 ± 0.00007	8.77	0.45625	97 ± 167	10	■	FR; $m = -2?$
$\Delta\Pi_{\text{mean}} \pm \sigma_{\Delta}$				264 ± 132			
<hr/>							
f_{237}	2.70471 ± 0.00012	3.63	0.36972		7	♦	?
f_{204}	2.69696 ± 0.00012	4.72	0.37079	92 ± 18	9	♦	?
f_{228}	2.69193 ± 0.00012	3.91	0.37148	60 ± 13	7	♦	?
f_{22}	2.68620 ± 0.00004	34.90	0.37227	68 ± 5	30	♦	?
$\Delta\Pi_{\text{mean}} \pm \sigma_{\Delta}$				73 ± 13			

are illustrated in the middle and lower panels, respectively. The period spacings and their deviation from the mean value, $\epsilon_{\Delta\Pi}$, are reported in Tables 3 & A1. For the prograde pattern in the frequency interval $(2.19$ to $2.90)$ d^{-1} , $\Delta\Pi$ decreases from 577 to 97 s with increasing period. Its mean period spacing equals $\Delta\Pi_{\text{mean},+} = 264 \pm 132$ s (the error is the standard deviation). There are several frequencies that are a combination of parent prograde g modes but do fit very well in the pattern (e.g. in the interval $(2.40$ to $2.47)$ d^{-1}). In addition, in the frequency interval $(2.68$ to $2.70)$ d^{-1} we detected a group of frequencies of much lower $\Delta\Pi_{\text{mean},+} = 73 \pm 13$ s that are well separated from the pre-cited prograde pattern. We show them with magenta diamonds in Fig. 5 (for the frequencies see Table 3). The retrograde modes in the frequency interval $(3.24$ to $4.79)$ d^{-1} have $\Delta\Pi_{\text{mean},+} = 226 \pm 137$ s (cyan circles in Fig. 5). However, some of these modes (in Table A1) are also combinations of prograde g modes (Saio et al. 2018). These combinations are listed in Table A2. For these modes, $\Delta\Pi$ increases from 20 to 491 s with

increasing period. The second group of retrograde modes was detected in the range $(1.66$ to $2.15)$ d^{-1} . They are illustrated by the green triangles in Fig. 5. Though the lower periods show a decreasing period spacing, we consider them to be part of the same group as discussed in Sec 5. The list of frequencies and their period spacing values are reported in Table A1. $\Delta\Pi$ in this pattern first decreases from 268 to 123 s and then increases from 28 to 565 s and its overall average is $\Delta\Pi_{\text{mean},+} = 162 \pm 130$ s. Similar to previous group of retrograde modes some of these modes are also a combination of prograde g modes (Table A2). Furthermore, we detected two more period spacing patterns (retrograde see Sec. 5) with a smaller number of detected modes than other detected modes. These modes are in the frequency intervals of $(1.58$ to $1.64)$ d^{-1} and $(5.82$ to $6.18)$ d^{-1} . They are illustrated with olive green pluses and orange stars, respectively, in Fig. 5. Their $\Delta\Pi$ values and errors are reported in Table A1. Their average period spacing values are $\Delta\Pi_{\text{mean},+} = 272 \pm 45$ s and $\Delta\Pi_{\text{mean},+} = 148 \pm 65$ s, respectively. We suggest that all detected

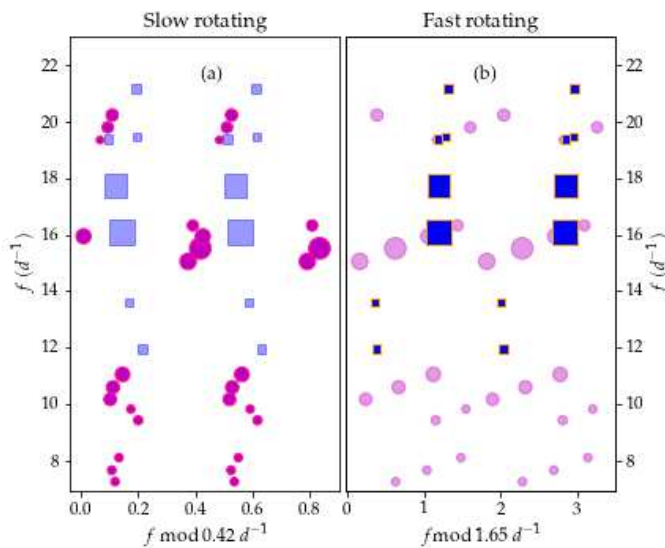


Fig. 4. Échelle diagram of p modes with (quasi)-regular frequency spacing from the Fourier spectrum of KIC 8975515 (Table 2). Symbol size refers to the amplitude of the p modes. Colour coding and symbols are similar to Fig. 3. (a) frequency modulo the mean rotational frequency spacing value associated to the slowly-rotating star, 0.419 d^{-1} (magenta circles) plotted twice. (b) frequency modulo the mean rotational frequency spacing value associated to the fast-rotating star, 1.654 d^{-1} (blue squares) plotted twice.

group of modes except the prograde g modes are r modes that are excited because of the fast rotation. We discuss this in details in Sec. 5. However, there are bunches of frequencies that occur at very low frequencies in the intervals $(0.1 \text{ and } 0.95) \text{ d}^{-1}$ and $(1.25 \text{ to } 1.55) \text{ d}^{-1}$. These modes are either a linear combination of prograde g modes ($nf_{gi} - mf_{gj}$, $n, m = 1, 2$ and i, j as index of the g modes) or prograde g modes and retrograde r modes f_8, f_{24} and f_{35} ($f_{gi} - f_{rj}$, i, j representing the g and r modes). Furthermore, there are a few frequencies lower than 0.1 d^{-1} . There are also a few significant frequencies in the frequency interval $(4.96 \text{ to } 5.82) \text{ d}^{-1}$. These frequencies are either a combination of prograde g modes ($nf_{gi} + mf_{gj}$) or a combination of prograde g and r modes ($af_{gi} + bf_{rj}$ and $a, b = 1, 2$). The combinations are listed in Table A2.

5. Discussion

5.1. The high-frequency modes

In the region $(7 \text{ to } 23.5) \text{ d}^{-1}$, we detected two kinds of multiplets that occur at both sides of the dominant frequency f_1 (13.97 d^{-1}), with frequency spacings $\Delta f_{\text{mean}} = 1.65$ and 0.42 d^{-1} . Both regular patterns (which appear in the form of doublets and triplets) are not perfectly symmetrical which could be indicative of second-order rotational effects (Saio 1981). To the first-order approximation, we have (Saio et al. 2015):

$$\langle P_{\text{rot}} \rangle = \frac{1}{\Delta f_{\text{rot}}} (1 - C_{n,\ell}) \quad (1)$$

where $C_{n,\ell}$ is the Ledoux constant (Ledoux 1951). For the p modes, the Ledoux constant $C_{n,\ell}$ is zero, and the rotation period is not related to the mode degree ℓ . Consequently, the rotation period that corresponds to the 1.65 d^{-1} and 0.42 d^{-1} splitting equals $P_{\text{rot}} = 0.604 \text{ d}$ and $P_{\text{rot}} = 2.385 \text{ d}$, respectively. $f_{200} (1.647 \pm 0.0001 \text{ d}^{-1})$ might be the rotation frequency of the

fast rotating star. The R value in Table 1 was obtained from blended photometry, however we know that both components have similar atmospheric properties, thus we may consider the value as a reasonable estimate for each component of the system. If we consider the radius $R = 2.197 R_{\odot}$ as an estimation of the radius for one of the components, we obtain equatorial velocities $V_{\text{eq}} \sim 182 \text{ km/s}$ and $\sim 46 \text{ km/s}$ and $i_{\text{rot}} \sim 63^\circ$ and $\sim 44^\circ$ for the fast and slowly-rotating stars, based on 1.65 d^{-1} and 0.42 d^{-1} splittings, respectively. The consistency between the spectroscopic projected rotational velocity and the one estimated from Δf_{mean} indicates that both components of the system may have p modes excited.

The three identified combinations of f_1 with either one of the prograde g modes or one of the retrograde r modes (Mode Couplings) suggests that f_1 , the prograde g and the retrograde r modes are excited in the fast-rotating component. f_1 is the most dominant frequency and a singlet in p mode region.

The échelle diagram of the detected p modes belonging to regular patterns shows that the ridges including the modes with different regular frequency splittings (0.42 and 1.65 d^{-1}) are crossing each other. This fact reveals these modes are originating from different companion stars (e.g. Li et al. 2018).

5.2. Regular period spacings of the g modes

Fig. 5 illustrates that the excited low-frequency modes include both prograde and retrograde modes. According to Saio et al. (2018) (Sec. 1) we may expect the r modes to appear as groups of low-frequency modes at frequencies slightly lower than m times the rotational frequency, $m f_{\text{rot}}$, for intermediate to fast-rotating stars. Effectively, for KIC 8975515, we found a close connection between the identified retrograde modes and the regular frequency spacing $\Delta f_{\text{mean}} = 1.654 \pm 0.018 \text{ d}^{-1}$ detected in the high-frequency region. The same conclusion holds for the two small series of frequencies with few modes (the stars and pluses in Fig. 5). The retrograde modes appear are in distinct period/frequency regions separated by the harmonics with respect to the harmonics of the (large) rotation frequency ($f_{200} = 1.647 \pm 0.0001 \text{ d}^{-1}$). Hence, we associated these modes to r modes and assigned an azimuthal order m to them according to their position with respect to boundaries of the type $\frac{1}{m f_{\text{rot}}}$. For instance, the r modes excited at the frequencies lower than 1.65 d^{-1} (from 1.54 to 1.64 d^{-1}) have been assigned to $m = 1$, and $m = 3$ r modes appear up to the period limit $\frac{1}{3 f_{\text{rot}}}$ from $(3.35$ to $4.94) \text{ d}^{-1}$. However, a few number of modes with much lower period spacing ($73 \pm 13 \text{ s}$) than all other detections are not located in an expected region following such interpretation. Thus, we cannot determine their origin and we did not detect any of them to be in regularly split patterns that could be associated to the rotational frequency of either component (or one of the components).

As expected from the models (e.g. Saio et al. 2018) the odd and even r modes display different structures: e.g., for r modes $m = 3$ the period spacing first increases from 71 s to 215 s and then decreases steeply to 69 s (periods from 0.216 to 0.223 d). In the immediately following period interval, the retrograde pattern starts with ΔP values increasing from 225 up to 491 s . However, no modes were detected beyond this range as evidence of the (expected) steep decrease of ΔP close to the period limit ($\frac{1}{2 f_{\text{rot}}}$). Beyond this period limit, the series of prograde g modes ($m = -2$) appear. In conclusion, we showed that an overwhelming majority of the detected low-frequency modes are located in period intervals which are largely delimited by integer multiples of the

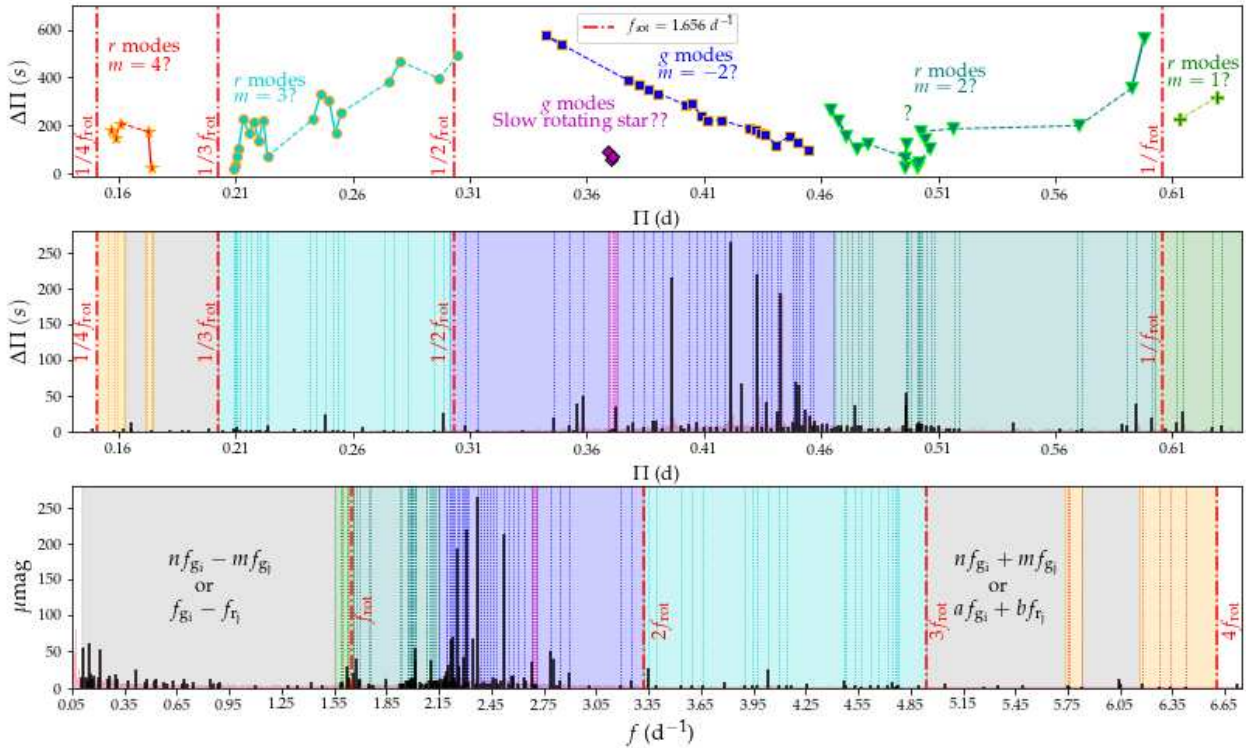


Fig. 5. (a) Period spacing patterns for r and g modes on the period spectrum of KIC 8975515 (LC). (b) The associated frequencies for the detected g/r modes in (a) (Tables 3 & A1) showed with pointed-lines in the same colour in panel (a). The frequencies in black are the significant modes and the full periodogram of KIC 8975515 is plotted in light pink.

rotation frequency of the fast-rotating star. This observational fact supports the conclusion that these r and g modes have the same origin as the series of p modes with $\Delta f_{\text{mean}} = 1.65 \text{ d}^{-1}$, i.e. they originate from the fast-rotating companion star.

6. Summary

We analysed a 4-year long dataset observed in long-cadence mode by the *Kepler* mission in order to study the pulsations of KIC 8975515. This target consists of a fast-rotating and a slowly rotating companion star (i.e. $v \sin i$ of $162 \pm 2 \text{ km/s}$ and $32 \pm 1 \text{ km/s}$) of otherwise similar masses and atmospheric properties. They form a SB2 system in a long-period and eccentric orbit. Binarity in combination with fast rotation of one of the companions along with hybrid pulsations makes this object of high asteroseismic interest.

The detailed pulsation analysis shows that the most dominant modes in the low- and high-frequency regime have about the same power. Concerning the low-frequency region of the frequency spectrum, the significant pulsation frequencies occur in the range $1.58 - 6.18 \text{ d}^{-1}$. We detected five regular period spacing patterns in this regime including a series of prograde g modes and four series of r modes ($m = 1, 2, 3$ and 4), well located in the frequency intervals delimited by the harmonics of the rotational frequency for the fast-rotating star.

We detected two types of combination frequencies in the lower-frequency region which are either a combination of prograde g modes or a combination of a g and a r mode. Both types appear at frequencies lower than $m=1$ up to 0.1 d^{-1} and in-between the $m=3$ and $m=4$ r modes. Some combinations also appear in the intermediate range from 6.72 to 8.63 d^{-1} . Concerning the high-frequency regime, the most dominant p mode f_1 (i.e. 13.97

d^{-1}) appears as a singlet between two groups of regularly split modes (20 modes between 7.24 and 21.17 d^{-1}) with Δf_{rot} equal to $0.419 \pm 0.020 \text{ d}^{-1}$ and $1.656 \pm 0.018 \text{ d}^{-1}$.

We interpreted both groups of p modes as multiplets of rotationally split p modes since their mean frequency spacings are in agreement with the estimated rotation velocity of each component. In addition, we detected the presence of the low frequency $f_{200} = 1.647 \pm 0.001 \text{ d}^{-1}$ whose value clearly agrees with the largest mean frequency spacing supporting the interpretation that it represents the rotation frequency of the fast-rotating star. Furthermore, we identified three combinations of f_1 with either one of the prograde g modes or one of the retrograde r modes, among the p modes. This indicates that f_1 has the same origin as the prograde g and the retrograde r modes, i.e. they all originate from the fast-rotating component. Finally, the échelle diagram of all the detected p mode frequencies versus each one of the mean spacings reveals that the modes associated to the different multiplets are located along crossing ridges, thus each multiplet comes from a different companion star. All of these conclusions put together along with the fact that the regions where the r and g modes appear as distinct groups with respect to the harmonics of the detected (fast) rotation frequency (f_{200}) show that we can identify the origin of most of the modes detected in KIC 8975515.

In summary, we propose on the basis of the presented study that the fast-rotating component is a hybrid (γ Dor- δ Sct) pulsator which also shows r modes of azimuthal order $m = 1, 2, 3$ and 4 naturally excited because of the fast rotation, while the slow-rotating companion is a δ Scuti pulsator with regularly (rotationally) split p modes.

Acknowledgements. The authors thank the *Kepler* team efforts to provide and present all the observational data and light curves for the public. The authors also appreciate and thank the *KASOC* team for presenting corrected light curves to the community. The authors acknowledge, the enlightening discussions with *Prof. Donald W. Kurtz* from Jeremiah Horrocks Institute, University of Central Lancashire, *Dr. Giovanni M. Mirouh* from Astrophysics Research Group, Faculty of Engineering and Physical Sciences, University of Surrey and *Prof. Omar Gustavo Benvenuto* from Universidad Nacional de La Plata, Buenos Aires, Argentina. A. S. also thanks *Paul Van Cauteren* from the Humain Observatory (ROB) for his continuous support. We also acknowledge the anonymous referee for very useful comments on the paper. We acknowledge the financial support of *ALMA-CONICYT grant number 31170029* for this research. Furthermore, P.J. acknowledges partial financial support of *FONDECYT Iniciación grant number 11170174*.

References

- Aerts, C., Christensen-Dalsgaard, J., & Kurtz, D. W. 2010, Asteroseismology
Antoci, V., Cunha, M., Houdek, G., et al. 2014, ApJ, 796, 118
Baglin, A., Auvergne, M., Barge, P., et al. 2006, in ESA Special Publication, Vol. 1306, The CoRoT Mission Pre-Launch Status - Stellar Seismology and Planet Finding, ed. M. Fridlund, A. Baglin, J. Lochard, & L. Conroy, 33
Balona, L. A., Daszyńska-Daszkiewicz, J., & Pamyatnykh, A. A. 2015, MNRAS, 452, 3073
Balona, L. A. & Dziembowski, W. A. 2011, MNRAS, 417, 591
Berthomieu, G. & Provost, J. 1983, A&A, 122, 199
Bouabid, M.-P., Dupret, M.-A., Salmon, S., et al. 2013, MNRAS, 429, 2500
Bowman, D. M. & Kurtz, D. W. 2018, MNRAS, 476, 3169
Bradley, P. A., Guzik, J. A., Miles, L. F., et al. 2015, AJ, 149, 68
Breger, M. 2007, Communications in Asteroseismology, 150, 25
Breger, M., Stich, J., Garrido, R., et al. 1993, A&A, 271, 482
Catelan, M. & Smith, H. A. 2015, Pulsating Stars ("Wiley-VCH")
Derekas, A., Murphy, S. J., Dálya, G., et al. 2019, MNRAS, 486, 2129
Duchêne, G. & Kraus, A. 2013, ARA&A, 51, 269
Dupret, M. A., Grigahcène, A., Garrido, R., et al. 2005, MNRAS, 360, 1143
Dupret, M.-A., Grigahcène, A., Garrido, R., Gabriel, M., & Scuflaire, R. 2004, A&A, 414, L17
Gaia Collaboration, Brown, A. G. A., Vallenari, A., et al. 2018a, A&A, 616, A1
Gaia Collaboration, Katz, D., Antoja, T., et al. 2018b, A&A, 616, A11
Gies, D. R., Matson, R. A., Guo, Z., et al. 2015, AJ, 150, 178
Guo, Z., Gies, D. R., & Matson, R. A. 2017, ApJ, 851, 39
Guzik, J. A., Kaye, A. B., Bradley, P. A., Cox, A. N., & Neuforge, C. 2000, ApJ, 542, L57
Hambleton, K. M., Kurtz, D. W., Prša, A., et al. 2013, MNRAS, 434, 925
Handler, G. 1999, MNRAS, 309, L19
Helminiak, K. G., Ukita, N., Kambe, E., et al. 2017, A&A, 602, A30
Houdek, G. 2000, Astronomical Society of the Pacific Conference Series, Vol. 210, Convective Effects on p-Mode Stability in δ Scuti Stars, ed. M. Breger & M. Montgomery, 454
Houdek, G., Balmforth, N. J., Christensen-Dalsgaard, J., & Gough, D. O. 1999, A&A, 351, 582
Keen, M. A., Bedding, T. R., Murphy, S. J., et al. 2015, MNRAS, 454, 1792
Koch, D. G., Borucki, W. J., Basri, G., & et al. 2010, ApJ, 713, L79
Kolbas, V., Pavlovskii, K., Southworth, J., et al. 2012, in IAU Symposium, Vol. 282, From Interacting Binaries to Exoplanets: Essential Modeling Tools, ed. M. T. Richards & I. Hubeny, 303–304
Kurtz, D. W., Saio, H., Takata, M., et al. 2014, MNRAS, 444, 102
Lampens, P., Frémant, Y., Vermeulen, L., et al. 2018, A&A, 610, A17
Ledoux, P. 1951, ApJ, 114, 373
Lee, J. W. 2016, ApJ, 833, 170
Li, G., Bedding, T. R., Murphy, S. J., et al. 2019a, MNRAS, 482, 1757
Li, G., Van Reeth, T., Bedding, T. R., Murphy, S. J., & Antoci, V. 2019b, MNRAS, 487, 782
Li, Y., Bedding, T. R., Li, T., et al. 2018, MNRAS, 476, 470
Lomb, N. R. 1976, Ap&SS, 39, 447
McNamara, D. H. 2000, in Astronomical Society of the Pacific Conference Series, Vol. 210, Delta Scuti and Related Stars, ed. M. Breger & M. Montgomery, 373
Miglio, A., Montalbán, J., Noels, A., & Eggenberger, P. 2008, MNRAS, 386, 1487
Mkrtchian, D. E., Lehmann, H., Rodríguez, E., et al. 2018, MNRAS, 475, 4745
Murphy, S. J., Bedding, T. R., Shibahashi, H., Kurtz, D. W., & Kjeldsen, H. 2014, MNRAS, 441, 2515
Murphy, S. J., Hey, D., Van Reeth, T., & Bedding, T. R. 2019, MNRAS, 485, 2380
Murphy, S. J., Moe, M., Kurtz, D. W., et al. 2018, MNRAS, 474, 4322
Ouazzani, R.-M., Salmon, S. J. A. J., Antoci, V., et al. 2017, MNRAS, 465, 2294
Qian, S.-B., Shi, X.-D., Zhu, L.-Y., et al. 2019, Research in Astronomy and Astrophysics, 19, 064
Ricker, G. R., Winn, J. N., Vanderspek, R., et al. 2015, Journal of Astronomical Telescopes, Instruments, and Systems, 1, 014003
Saio, H. 1981, ApJ, 244, 299
Saio, H. 1982, ApJ, 256, 717
Saio, H., Bedding, T. R., Kurtz, D. W., et al. 2018, MNRAS, 477, 2183
Saio, H., Kurtz, D. W., Takata, M., et al. 2015, MNRAS, 447, 3264
Samadi-Ghadim, A., Jassur, D. M. Z., Nassiri, S., et al. 2010, New A, 15, 339
Samadi-Ghadim, A., Lampens, P., & Jassur, D. 2018a, Acta Astron., 68, 425
Samadi-Ghadim, A., Lampens, P., & Jassur, D. 2018b, MNRAS, 474, 5549
Sánchez Arias, J. P., Cósico, A. H., & Althaus, L. G. 2017, A&A, 597, A29
Scargle, J. D. 1982, ApJ, 263, 835
Schmid, V. S., Tkachenko, A., Aerts, C., et al. 2015, A&A, 584, A35
Shibahashi, H. 1979, PASJ, 31, 87
Tassoul, M. 1980, ApJS, 43, 469
Uytterhoeven, K., Moya, A., Grigahcène, A., et al. 2011, A&A, 534, A125
Van Reeth, T., Tkachenko, A., & Aerts, C. 2016, A&A, 593, A120
Vaníček, P. 1971, Ap&SS, 12, 10
Xiong, D. R., Deng, L., Zhang, C., & Wang, K. 2016, MNRAS, 457, 3163
Zhang, X. B., Fu, J. N., Luo, C. Q., Ren, A. B., & Yan, Z. Z. 2018, ApJ, 865, 115
Zwintz, K., Fossati, L., Ryabchikova, T., et al. 2014, Science, 345, 550

Table A1. Detected r modes in the Fourier spectrum of KIC 8975515 which are located at lower frequencies equal, two and three times ($m = 1, 2, 3$) of the observational rotational frequency $f_{\text{rot}} = 1.65 \text{ d}^{-1}$ (Fig. 3 & Table 2) associated to the fast rotating star ($v \sin i = 162 \text{ kms}$). *FR* denotes that the mode originality is from the *Fast Rotating* star. The determined azimuthal order m is based on $f_{\text{r mode}} = m f_{\text{rot}}$. The color coding and symbols are similar to Fig. 5. $\epsilon_{\Delta\Pi}$ is the deviation value in seconds from $\Delta\Pi_{\text{mean}}$ in each series, that is large due to the retrograde nature of period spacing pattern. The variance error ϵ_{var} for all of $\Delta\Pi$ is of the order of 10^{-5} sec for each $\Delta\Pi$.

f_i	$f \pm \epsilon_f$ d^{-1}	A μmag	Π d	$\Delta\Pi \pm \epsilon_{\Delta\Pi}$ s	SNR	color Fig. 5	comment
f_{57}	1.63391 ± 0.00006	13.63	0.61203		15	+	FR, $m = 1$
f_{24}	1.62692 ± 0.00004	29.96	0.61466	227 ± 45	31	+	FR, $m = 1$
f_{135}	1.59456 ± 0.00009	7.14	0.62713		11	+	FR, $m = 1$
f_{112}	1.58529 ± 0.00008	8.57	0.63080	317 ± 45	12	+	FR, $m = 1$
			$\Delta\Pi_{\text{mean}} \pm \sigma_{\Delta}$	272 ± 45			
f_{126}	2.14759 ± 0.00008	7.31	0.46564		9	▲	FR, $m = 2$
f_{101}	2.13337 ± 0.00007	9.10	0.46874	268 ± 88	10	▲	FR, $m = 2$
f_{105}	2.12180 ± 0.00007	9.01	0.47130	221 ± 40	10	▲	FR, $m = 2$
f_{120}	2.11381 ± 0.00008	7.80	0.47308	154 ± 26	9	▲	FR, $m = 2$
f_{93}	2.10223 ± 0.00007	9.78	0.47569		11	▲	FR, $m = 2$
f_{102}	2.09705 ± 0.00007	9.08	0.47686	101 ± 79	11	▲	FR, $m = 2$
f_{197}	2.07472 ± 0.00009	4.84	0.48199		6	▲	FR, $m = 2$
f_{189}	2.08089 ± 0.00009	5.09	0.48056	123 ± 57	7	▲	FR, $m = 2$
f_{14}	2.01581 ± 0.00002	55.08	0.49608		30	▲	FR, $m = 2$
f_{21}	2.01453 ± 0.00003	36.98	0.49639	27 ± 135	31	▲	FR, $m = 2$
f_{169}	2.01162 ± 0.00009	5.74	0.49711	62 ± 100	8	▲	FR, $m = 2$
f_{165}	2.00579 ± 0.00009	5.87	0.49856	125 ± 37	8	▲	FR, $m = 2$
f_{70}	1.99527 ± 0.00006	11.55	0.50119		12	▲	FR, $m = 2$
f_{52}	1.99395 ± 0.00005	14.63	0.50152	28 ± 152	13	▲	FR, $m = 2$
f_{64}	1.99256 ± 0.00006	12.47	0.50187	30 ± 150	13	▲	FR, $m = 2$
f_{69}	1.99033 ± 0.00006	11.77	0.50243	49 ± 131	13	▲	FR, $m = 2$
f_{65}	1.98707 ± 0.00006	12.43	0.50325		12	▲	FR, $m = 2$
f_{111}	1.97919 ± 0.00007	8.68	0.50526	173 ± 7	11	▲	FR, $m = 2$
f_{97}	1.97265 ± 0.00007	9.50	0.50693	145 ± 36	11	▲	FR, $m = 2$
f_{133}	1.96789 ± 0.00008	7.15	0.50816	106 ± 74	9	▲	FR, $m = 2$
f_{170}	1.93403 ± 0.00009	5.67	0.51705		8	▲	FR, $m = 2$
f_{199}	1.92603 ± 0.00009	4.82	0.51920	186 ± 6	6	▲	FR, $m = 2$
f_{227}	1.75720 ± 0.00010	4.04	0.56909		6	▲	FR, $m = 2$
f_{188}	1.75012 ± 0.00010	5.15	0.57139	199 ± 18	8	▲	FR, $m = 2$
f_{100}	1.69309 ± 0.00007	9.25	0.59064	355 ± 75	12	▲	FR, $m = 2$
f_{18}	1.68141 ± 0.00003	40.58	0.59474		30	▲	FR, $m = 2$
f_{35}	1.66312 ± 0.00005	21.41	0.60128	565 ± 385	27	▲	FR, $m = 2$
			$\Delta\Pi_{\text{mean}} \pm \sigma_{\Delta}$	162 ± 130			
f_{96}	3.24975 ± 0.00009	9.60	0.30772		22	●	FR; $m = 3$
f_{246}	3.19086 ± 0.00016	3.15	0.31340	491 ± 265	8	●	FR; $m = 3$
f_{26}	3.34565 ± 0.00005	26.76	0.29890		30	●	FR, $m = 3$
f_{245}	3.39771 ± 0.00016	3.30	0.29432	396 ± 170	8	●	FR, $m = 3$
f_{239}	3.53266 ± 0.00016	3.41	0.28307	468 ± 242	9	●	FR, $m = 3$
f_{257}	3.60157 ± 0.00015	2.77	0.27766		6	●	FR, $m = 3$
f_{238}	3.65986 ± 0.00017	3.42	0.27323	382 ± 156	9	●	FR, $m = 3$
f_{264}	3.89928 ± 0.00016	2.55	0.25646		6	●	FR, $m = 3$
f_{267}	3.94425 ± 0.00017	2.49	0.25353	253 ± 27	6	●	FR, $m = 3$
f_{224}	3.97494 ± 0.00015	4.22	0.25158	169 ± 57	11	●	FR, $m = 3$
f_{27}	4.03130 ± 0.00005	25.12	0.24806	304 ± 78	30	●	FR, $m = 3$
f_{266}	4.09437 ± 0.00017	2.51	0.24424	330 ± 104	6	●	FR, $m = 3$
f_{254}	4.13855 ± 0.00018	2.84	0.24163	225 ± 14	8	●	FR, $m = 3$
f_{104}	4.46643 ± 0.00012	9.03	0.22389		25	●	FR, $m = 3$
f_{265}	4.48252 ± 0.00020	2.52	0.22309	69 ± 156	7	●	FR, $m = 3$
f_{230}	4.53511 ± 0.00017	3.86	0.22050	223 ± 2	12	●	FR, $m = 3$
f_{273}	4.56792 ± 0.00019	2.26	0.21892	137 ± 89	6	●	FR, $m = 3$
f_{232}	4.62042 ± 0.00017	3.78	0.21643	215 ± 11	11	●	FR, $m = 3$

Table A1. continued.

f_i	$f \pm \epsilon_f$ d^{-1}	A μmag	Π d	$\Delta\Pi \pm \epsilon_{\Delta\Pi}$ s	SNR	color Fig. 5	comment
f_{250}	4.66278 ± 0.00020	2.94	0.21446	170 ± 56	9	●	FR, $m = 3$
f_{253}	4.72084 ± 0.00019	2.85	0.21183	228 ± 2	8	●	FR, $m = 3$
f_{139}	4.74841 ± 0.00012	6.94	0.21060	106 ± 120	19	●	FR, $m = 3$
f_{276}	4.76692 ± 0.00019	2.23	0.20978	71 ± 155	6	●	FR, $m = 3$
f_{236}	4.77578 ± 0.00018	3.67	0.20939	34 ± 192	12	●	FR, $m = 3$
f_{221}	4.78114 ± 0.00017	4.29	0.20916	20 ± 205	13	●	FR, $m = 3$
$\Delta\Pi_{\text{mean}} \pm \sigma_{\Delta}$				226 ± 137			
f_{293}	6.17774 ± 0.00014	6.14	0.16187		22	*	FR, $m = 4$
f_{293}	6.27130 ± 0.00023	1.83	0.15946	209 ± 60	6	*	FR, $m = 4$
f_{271}	6.34149 ± 0.00025	2.31	0.15769	153 ± 4	9	*	FR, $m = 4$
f_{293}	6.42793 ± 0.00023	1.82	0.15557	183 ± 35	6	*	FR, $m = 4$
f_{261}	5.74977 ± 0.00022	2.66	0.17392		9	*	FR, $m = 4$
f_{287}	5.75903 ± 0.00021	1.97	0.17364	24 ± 124	6	*	FR, $m = 4$
f_{290}	5.82624 ± 0.00022	1.92	0.17164	173 ± 25	6	*	FR, $m = 4$
$\Delta\Pi_{\text{mean}} \pm \sigma_{\Delta}$				148 ± 65			

Table A2. Detected frequencies with acceptable signal-to-noise ratio (SNR) from the Fourier spectrum of KIC 8975515 (Long Cadence observations, LC). P : parent frequencies (Sec.4), SR/FR: detected $g/r/p$ modes are most probably associated to Slow Rotating/Fast Rotating star. PS : detected g/r mode is part of a prograde/retrograde Period Spacing pattern. FS : detected $g/r/p$ mode is with (semi-)regularly spaced from the other frequency in the same multiplet. MC : mode is excited as the result of coupling of the most dominant detected p mode (f_1) and a detected g/r mode ($f_1 \pm f_{g,r}$). The superscript "*" denotes the frequencies that are not formed from a *unique* combination of parent frequencies. m is determined based on $f_{\text{mode}} = m f_{\text{rot}}$. ℓ is the mode degree and is determined based on observed rotational splitting of a low-/high-frequency mode.

f_i	$f \pm \epsilon_f$ d^{-1}	$A \pm \epsilon_A$ μmag	Π d	SNR	P	PS	FS	mode	m	FR/SR	comb.	MC	ref.
f_1	13.97236±0.00001	267.74±4.62	0.07157	204				p	0?	FR			
f_2	2.37418±0.00001	264.99±5.31	0.42120	76	✓	✓		g	-2?	FR			Table 3 & Fig. 5
f_3	2.31022±0.00001	219.12±3.99	0.43286	78	✓	✓		g	-2?	FR			Table 3 & Fig. 5
f_4	2.52345±0.00001	213.96±4.68	0.39628	70	✓	✓		g	-2?	FR			Table 3 & Fig. 5
f_5	2.25761±0.00001	194.15±3.28	0.44295	80	✓	✓		g	-2?	FR			Table 3 & Fig. 5
f_6	16.07633±0.00002	128.14±5.18	0.06220	76			✓	p		FR			Table 2 & Fig. 3
f_7	17.73452±0.00002	84.42±5.62	0.05639	76			✓	p		FR			Table 2 & Fig. 3
f_8	2.22490±0.00002	70.43±3.45	0.44946	30	✓	✓		g		FR			
f_9	15.51470±0.00003	68.71±5.96	0.06446	76			✓	p		SR			Table 2 & Fig. 3
f_{10}	2.34658±0.00002	67.83±3.51	0.42615	30	✓								
f_{11}	2.21884±0.00002	65.65±3.34	0.45069	30	✓	✓		g		FR			
f_{12}	0.14929±0.00002	61.22±2.73	6.69859	24							$f_4 - f_2^*$		
f_{13}	0.11657±0.00002	55.88±2.38	8.57853	24							$f_2 - f_5$		
f_{14}	2.01581±0.00002	55.08±3.27	0.49608	30	✓	✓		r	2?	FR			Table A1 & Fig. 5
f_{15}	0.21323±0.00002	54.15±2.26	4.68984	23							$f_3 - f_4$		
f_{16}	2.78938±0.00003	51.37±3.65	0.35850	30	✓								
f_{17}	2.28902±0.00003	41.86±3.25	0.43687	30	✓	✓		g	-2?	FR			Table 3 & Fig. 5
f_{18}	1.68141±0.00003	40.58±3.24	0.59474	30	✓	✓	✓	r	2?	FR			Table A1 & Fig. 5
f_{19}	2.80931±0.00003	39.39±3.64	0.35596	30	✓								
f_{20}	2.10835±0.00003	37.96±3.14	0.47431	31	✓								
f_{21}	2.01453±0.00003	36.98±3.17	0.49639	30	✓	✓		r	2?	FR			Table A1 & Fig. 5
f_{22}	2.68620±0.00004	34.90±3.27	0.37227	30	✓	✓		?		?			Table 3 & Fig. 5
f_{23}	2.20487±0.00004	30.55±2.92	0.45354	27	✓								
f_{24}	1.62692±0.00004	29.96±3.16	0.61466	30	✓	✓		r	1?	FR			Table A1 & Fig. 5
f_{25}	2.26457±0.00004	28.55±2.93	0.44158	27	✓	✓		g	-2?	FR			Table 3 & Fig. 5
f_{26}	3.34565±0.00005	26.76±3.65	0.29890	30		✓		r	3?	FR			Table A1 & Fig. 5
f_{27}	4.03130±0.00005	25.12±3.66	0.24806	30		✓		r	3?	FR		$2f_{14}$	Table A1 & Fig. 5
f_{28}	7.83244±0.00005	24.75±3.51	0.12767	30							$2f_{17} + 2f_{24}^*$		
f_{29}	21.90413±0.00009	24.31±6.06	0.04565	76									
f_{30}	0.41522±0.00003	24.23±1.94	2.40836	12							$f_{16} - f_2^*$		
f_{31}	2.19728±0.00004	23.44±2.26	0.45511	21	✓								
f_{32}	15.05250±0.00006	22.82±3.42	0.06643	30			✓	p		SR			Table 2 & Fig. 3
f_{33}	20.16104±0.00006	22.32±3.36	0.04960	30									
f_{34}	4.03244±0.00006	22.22±3.32	0.24799	30									
f_{35}	1.66312±0.00005	21.41±2.90	0.60128	27	✓	✓		r	2?	FR			Table A1 & Fig. 5
f_{36}	15.02827±0.00006	21.20±3.47	0.06654	30									
f_{37}	2.89346±0.00006	20.83±3.23	0.34561	30	✓	✓		g	-2?	FR			Table 3 & Fig. 5

Table A2. continued.

f_i	$f \pm \epsilon_f$ d^{-1}	$A \pm \epsilon_A$ μmag	Π	SNR	P	PS	FS	mode	m	FR/SR	comb.	MC	ref.
f_{38}	13.97148±0.00007	19.96±3.54	0.07157	30									
f_{39}	0.15528±0.00003	18.83±1.63	6.43987	9							$f_2 - f_{11}$		
f_{40}	13.97325±0.00007	18.18±3.57	0.07157	30	✓			g	-2?	FR			Table 3 & Fig. 5
f_{41}	0.29854±0.00003	17.61±1.59	3.34966	8							$2f_2 - 2f_4^*$		
f_{42}	2.57491±0.00005	16.79±2.23	0.38836	21									
f_{43}	2.56869±0.00005	16.50±2.24	0.38930	21	✓								
f_{44}	0.17690±0.00003	16.40±1.49	5.65280	8							$f_2 - f_{31}^*$		
f_{45}	15.94343±0.00008	16.27±3.62	0.06272	30		✓		p		SR			Table 2 & Fig. 3
f_{46}	2.18588±0.00005	15.63±2.07	0.45748	14							$2f_8 - f_{25}$		
f_{47}	0.26580±0.00004	15.52±1.50	3.76224	8							$f_2 - f_{20}$		
f_{48}	2.01358±0.00005	15.00±2.08	0.49663	14							$2f_{21} - f_{14}$		
f_{49}	2.45825±0.00005	14.90±2.10	0.40679	14	✓			g	-2?	FR			Table 3 & Fig. 5
f_{50}	2.23396±0.00005	14.84±2.06	0.44764	14									
f_{51}	11.04825±0.00009	14.65±3.63	0.09051	30		✓	✓	p		SR			Table 2 & Fig. 3
f_{52}	1.99395±0.00005	14.63±1.98	0.50152	12	✓			r	2?	FR			Table A1 & Fig. 5
f_{53}	0.10755±0.00003	14.62±1.31	9.29759	7									
f_{54}	2.63465±0.00006	14.21±2.15	0.37956	18	✓			g	2?	FR			Table 3 & Fig. 5
f_{55}	0.12792±0.00004	14.20±1.40	7.81756	7									
f_{56}	0.20199±0.00003	13.69±1.21	4.95070	6							$f_{10} - f_{11}$		
f_{57}	1.63391±0.00006	13.63±2.11	0.61203	14	✓			r	1?	FR			Table A1 & Fig. 5
f_{58}	0.10941±0.00004	13.57±1.30	9.14017	7							$f_2 - f_{31}^*$		
f_{59}	2.01671±0.00006	13.46±2.00	0.49586	12							$2f_{14} - f_{21}$		
f_{60}	6.04730±0.00009	13.12±3.27	0.16536	30							$3f_{14}$		
f_{61}	1.84437±0.00006	13.06±2.05	0.54219	14									
f_{62}	2.16094±0.00006	12.81±2.05	0.46276	14							$2f_8 - f_{17}$		
f_{63}	1.69976±0.00006	12.72±2.06	0.58832	14							$2f_{35} - f_{24}$		
f_{64}	1.99256±0.00006	12.47±1.96	0.50187	12	✓			r	2?	FR			Table A1 & Fig. 5
f_{65}	1.98707±0.00006	12.43±1.88	0.50325	12	✓			r	2?	FR			Table A1 & Fig. 5
f_{66}	0.47916±0.00005	11.92±1.47	2.08697	8							$f_3 - f_{16}$		
f_{67}	0.25885±0.00004	11.89±1.26	3.86324	7							$f_3 - f_{43}$		
f_{68}	0.30455±0.00004	11.85±1.27	3.28350	7							$f_4 - f_{11}^*$		
f_{69}	1.99033±0.00006	11.77±1.98	0.50243	12	✓			r	2?	FR			Table A1 & Fig. 5
f_{70}	1.99527±0.00006	11.55±1.83	0.50119	12	✓			r	2?	FR			Table A1 & Fig. 5
f_{71}	0.20089±0.00004	11.53±1.21	4.97788	6							$f_{10} - f_{42}$		
f_{72}	2.47839±0.00007	11.37±1.99	0.40349	12	✓			g	2?	FR	$2f_4 - f_{43}$		Table 3 & Fig. 5
f_{73}	0.16947±0.00004	11.18±1.20	5.90074	6							$f_2 - f_{23}$		
f_{74}	0.69282±0.00006	11.14±1.88	1.44338	12							$f_2 - f_{18}$		
f_{75}	0.84205±0.00007	11.12±2.03	1.18758	14							$f_4 - f_{18}$		
f_{76}	2.17244±0.00007	11.11±1.97	0.46031	12									
f_{77}	0.11873±0.00004	11.04±1.14	8.42236	6							$2f_{23} - 2f_{25}$		
f_{78}	0.53188±0.00005	11.03±1.61	1.88012	8							$f_5 - f_{16}^*$		
f_{79}	20.92536±0.00012	11.03±3.65	0.04779	30									

Article number, page 14 of 19
Table A2. continued.

f_i	$f \pm \epsilon_f$ d^{-1}	$A \pm \epsilon_A$ μmag	Π	SNR	P	PS	FS	mode	m	FR/SR	comb.	MC	ref.
f_{80}	0.13599 ± 0.00004	10.94 ± 1.18	7.35343	6									
f_{81}	16.07544 ± 0.00013	10.65 ± 3.67	0.06221	30									
f_{82}	2.14092 ± 0.00006	10.57 ± 1.82	0.46709	12									
f_{83}	0.62882 ± 0.00006	10.54 ± 1.67	1.59028	10	✓			g	-2?	FR	$2f_5 - f_2$		Table 3 & Fig. 5
f_{84}	1.98588 ± 0.00006	10.50 ± 1.78	0.50356	11									
f_{85}	0.51928 ± 0.00005	10.43 ± 1.46	1.92575	8									
f_{86}	2.50014 ± 0.00007	10.43 ± 1.96	0.39998	12									
f_{87}	0.37001 ± 0.00004	10.35 ± 1.23	2.70264	7									
f_{88}	2.01958 ± 0.00006	10.35 ± 1.79	0.49515	11									
f_{89}	1.99180 ± 0.00006	10.29 ± 1.77	0.50206	11									
f_{90}	1.95897 ± 0.00007	10.20 ± 1.78	0.51047	11									
f_{91}	16.07721 ± 0.00013	10.20 ± 3.67	0.06220	30									
f_{92}	2.64890 ± 0.00008	9.96 ± 2.06	0.37752	14									
f_{93}	2.10223 ± 0.00007	9.78 ± 1.72	0.47569	11	✓			r	2?	FR			Table A1 & Fig. 5
f_{94}	10.59499 ± 0.00013	9.72 ± 3.35	0.09438	30		✓		p		SR	$f_5 - f_{35}$	✓	Table 2 & Fig. 3
f_{95}	2.83861 ± 0.00008	9.61 ± 2.12	0.35229	14	✓			g	-2?	FR			Table 3 & Fig. 5
f_{96}	3.24975 ± 0.00009	9.60 ± 2.25	0.30772	21									
f_{97}	1.97265 ± 0.00007	9.50 ± 1.77	0.50693	11	✓			r	2?	FR			Table A1 & Fig. 5
f_{98}	0.52977 ± 0.00006	9.47 ± 1.41	1.88761	7									
f_{99}	2.22625 ± 0.00007	9.35 ± 1.67	0.44919	10									
f_{100}	1.69309 ± 0.00007	9.25 ± 1.83	0.59064	12	✓			r	2?	FR	$2f_3 - 2f_4$		Table A1 & Fig. 5
f_{101}	2.13337 ± 0.00007	9.10 ± 1.63	0.46874	9	✓			r	2?	FR	$2f_5 - f_{17}$		Table A1 & Fig. 5
f_{102}	2.09705 ± 0.00007	9.08 ± 1.72	0.47686	11	✓			r	2?	FR	$2f_3 - f_4$		Table A1 & Fig. 5
f_{103}	2.10931 ± 0.00007	9.05 ± 1.65	0.47409	9									
f_{104}	4.46643 ± 0.00012	9.03 ± 2.82	0.22389	24	✓			r	3?	FR			Table A1 & Fig. 5
f_{105}	2.12180 ± 0.00007	9.01 ± 1.68	0.47130	10	✓			r	2?	FR			Table A1 & Fig. 5
f_{106}	2.17351 ± 0.00007	8.83 ± 1.65	0.46009	10									
f_{107}	2.21165 ± 0.00007	8.82 ± 1.70	0.45215	10									
f_{108}	0.89650 ± 0.00008	8.78 ± 1.82	1.11545	12									
f_{109}	2.19179 ± 0.00007	8.77 ± 1.64	0.45625	9									
f_{110}	2.17933 ± 0.00007	8.73 ± 1.71	0.45886	10									
f_{111}	1.97919 ± 0.00007	8.68 ± 1.71	0.50526	10	✓			r	2?	FR	$f_4 - f_{24}$		Table A1 & Fig. 5
f_{112}	1.58529 ± 0.00008	8.57 ± 1.83	0.63080	12	✓			r	1?	FR	$f_5 - 2f_8$		Table A1 & Fig. 5
f_{113}	2.25232 ± 0.00008	8.47 ± 1.73	0.44399	11									
f_{114}	0.74722 ± 0.00007	8.38 ± 1.63	1.33830	9									
f_{115}	2.01813 ± 0.00007	8.22 ± 1.63	0.49551	9									
f_{116}	10.16604 ± 0.00015	8.08 ± 3.27	0.09837	30		✓		p		SR			Table 2 & Fig. 3
f_{117}	1.98238 ± 0.00008	7.98 ± 1.64	0.50444	9									
f_{118}	0.63066 ± 0.00007	7.85 ± 1.41	1.58564	7									
f_{119}	17.73366 ± 0.00016	7.83 ± 3.34	0.05639	30									
f_{120}	2.11381 ± 0.00008	7.80 ± 1.58	0.47308	9	✓			r	2?	FR			Table A1 & Fig. 5
f_{121}	2.14311 ± 0.00008	7.79 ± 1.63	0.46661	9									

Table A2. continued.

f_i	$f \pm \epsilon_f$ d^{-1}	$A \pm \epsilon_A$ μmag	Π d	SNR	P	PS	FS	mode	m	FR/SR	comb.	MC	ref.
f_{122}	2.24114±0.00008	7.54±1.59	0.44620	9									
f_{123}	0.57616±0.00006	7.47±1.22	1.73564	6							$f_5 - f_{18}$		
f_{124}	3.78867±0.00011	7.41±2.15	0.26394	18									
f_{125}	0.46577±0.00006	7.36±1.11	2.14698	5									
f_{126}	2.14759±0.00008	7.31±1.57	0.46564	9	✓			r	2?	FR			Table A1 & Fig. 5
f_{127}	20.23788±0.00017	7.31±3.29	0.04941	30		✓		p		SR			Table 2 & Fig. 3
f_{128}	1.98816±0.00008	7.24±1.46	0.50298	8		✓		g	-2?	FR	$f_4 - f_8$		Table 3 & Fig. 5
f_{129}	2.29919±0.00008	7.23±1.52	0.43494	8	✓						$2f_{22} - 2f_{24}$		
f_{130}	2.111842±0.00008	7.20±1.57	0.47205	9									
f_{131}	2.26535±0.00008	7.20±1.57	0.44143	9									
f_{132}	17.73542±0.00017	7.18±3.26	0.05638	30									
f_{133}	1.96789±0.00008	7.15±1.58	0.50816	9	✓			r	2?	FR			Table A1 & Fig. 5
f_{134}	15.98439±0.00017	7.15±3.28	0.06256	30									
f_{135}	1.59456±0.00009	7.14±1.71	0.62713	10	✓			r	1?	FR			Table A1 & Fig. 5
f_{136}	1.41664±0.00010	7.00±1.83	0.70590	12									
f_{137}	2.19374±0.00009	7.00±1.61	0.45584	8									
f_{138}	2.45944±0.00009	6.98±1.61	0.40660	8							$2f_2 - f_{17}$		
f_{139}	4.74841±0.00012	6.94±2.16	0.21060	18	✓			r	3?	FR	$f_4 + f_8; 2f_2$		Table A1 & Fig. 5
f_{140}	2.32178±0.00008	6.93±1.56	0.43070	9	✓			g	-2?	FR			Table 3 & Fig. 5
f_{141}	1.98096±0.00009	6.90±1.61	0.50481	8									
f_{142}	1.97613±0.00008	6.83±1.51	0.50604	8							$f_4 - f_{37}$		
f_{143}	2.40690±0.00009	6.77±1.56	0.41547	9	✓			g	-2?	FR	$2f_5 - f_{20}$		Table 3 & Fig. 5
f_{144}	2.04439±0.00009	6.74±1.56	0.48914	9									
f_{145}	7.35852±0.00016	6.70±2.93	0.13590	27							$2f_{14} + 2f_{35}$		
f_{146}	2.43813±0.00009	6.69±1.58	0.41015	9	✓			g	-2?	FR	$2f_2 - f_3$		Table 3 & Fig. 5
f_{147}	2.60372±0.00009	6.69±1.67	0.38407	10	✓			g	-2?	FR			Table 3 & Fig. 5
f_{148}	1.95637±0.00008	6.51±1.47	0.51115	8									
f_{149}	2.36004±0.00009	6.48±1.57	0.42372	9							$2f_{42} - f_{16}^*$		
f_{150}	0.67918±0.00007	6.47±1.22	1.47237	6							$2f_{10} - 2f_{22}$		
f_{151}	2.15726±0.00008	6.43±1.41	0.46355	7							$2f_{24} - f_{42}$		
f_{152}	2.42171±0.00009	6.43±1.51	0.41293	8	✓			g	-2?	FR	$f_4 - f_{35}^*$		Table 3 & Fig. 5
f_{153}	0.86029±0.00009	6.42±1.62	1.16239	8									
f_{154}	2.111310±0.00009	6.42±1.51	0.47324	8									
f_{155}	0.59452±0.00007	6.37±1.11	1.68202	5									
f_{156}	6.72024±0.00016	6.23±2.61	0.14880	24							$f_3 + 2f_{23}^*$		
f_{157}	2.54831±0.00010	6.18±1.57	0.39242	9	✓			g	-2?	FR			Table 3 & Fig. 5
f_{158}	2.13573±0.00009	6.17±1.41	0.46822	7									
f_{159}	6.17774±0.00014	6.14±2.23	0.16187	21							$2f_5 + 2f_{35}$		
f_{160}	2.25033±0.00009	6.13±1.51	0.44438	8							$2f_{42} - f_{25}$		
f_{161}	2.19934±0.00009	6.07±1.47	0.45468	8									
f_{162}	2.19103±0.00009	5.98±1.46	0.45641	8							$2f_{23} - f_{11}$		
f_{163}	1.94088±0.00009	5.94±1.46	0.51523	8							$2f_5 - f_{42}$		

Table A2. continued.

Table A2. continued.

f_i	$f \pm \epsilon_f$ d^{-1}	$A \pm \epsilon_A$ μmag	Π d	SNR	P	PS	FS	mode	m	FR/SR	comb.	MC	ref.
f_{207}	1.96217±0.00009	4.58±1.14	0.50964	6									
f_{208}	1.99649±0.00009	4.55±1.11	0.50088	5									
f_{209}	2.21260±0.00009	4.55±1.10	0.45196	5									
f_{210}	2.49083±0.00011	4.54±1.33	0.40147	7							$2f_{11} - f_8^*$		
f_{211}	20.45416±0.00024	4.54±2.94	0.04889	27							$2f_2 - f_5$		
f_{212}	1.48172±0.00012	4.49±1.38	0.67489	7									
f_{213}	1.28700±0.00012	4.48±1.41	0.77700	7									
f_{214}	2.25609±0.00009	4.40±1.10	0.44325	6									
f_{215}	1.77839±0.00010	4.37±1.12	0.56231	6									
f_{216}	2.06446±0.00009	4.37±1.10	0.48439	6									
f_{217}	2.30884±0.00010	4.35±1.14	0.43312	6									
f_{218}	1.67856±0.00010	4.31±1.13	0.59575	6							$2f_{42} - f_{17}$		
f_{219}	2.27908±0.00010	4.30±1.10	0.43877	6	✓			g	-2?	FR			Table 3 & Fig. 5
f_{220}	1.70286±0.00010	4.29±1.13	0.58725	6									
f_{221}	4.78114±0.00017	4.29±1.92	0.20916	13	✓			r	3?	FR	$f_4 + f_5$		Table A1 & Fig. 5
f_{222}	11.11326±0.00020	4.29±2.26	0.08998	21									
f_{223}	1.34210±0.00012	4.22±1.35	0.74510	7									
f_{224}	3.97494±0.00015	4.22±1.73	0.25158	11	✓			r	3?	FR			Table A1 & Fig. 5
f_{225}	6.04646±0.00018	4.17±2.06	0.16539	14							$2f_{14} + 2f_{21}$		
f_{226}	21.76370±0.00026	4.16±2.93	0.04595	27									
f_{227}	1.75720±0.00010	4.04±1.10	0.56909	5	✓			r	2?	FR	$2f_{14} - 2f_{37}$		Table A1 & Fig. 5
f_{228}	2.69193±0.00012	3.91±1.25	0.37148	7	✓			?	?		?		Table 3 & Fig. 5
f_{229}	2.82110±0.00013	3.88±1.37	0.35447	7									
f_{230}	4.53511±0.00017	3.86±1.77	0.22050	11	✓			r	3?	FR	$f_3 + f_8$		Table A1 & Fig. 5
f_{231}	4.02823±0.00015	3.81±1.57	0.24825	9									
f_{232}	4.62042±0.00017	3.78±1.71	0.21643	10	✓			r	3?	FR	$f_{10} + f_{18}; 2f_3$		Table A1 & Fig. 5
f_{233}	1.10075±0.00011	3.77±1.14	0.90847	6							$2f_{35} - f_8$		
f_{234}	4.89775±0.00018	3.74±1.79	0.20418	11							$f_2 + f_4^*$		
f_{235}	5.34932±0.00019	3.74±1.88	0.18694	12									
f_{236}	4.77578±0.00018	3.67±1.77	0.20939	11	✓			r	3?	FR			Table A1 & Fig. 5
f_{237}	2.70471±0.00012	3.63±1.21	0.36972	6	✓			?	?		?		Table 3 & Fig. 5
f_{238}	3.65986±0.00017	3.42±1.51	0.27323	8	✓			r	3?	FR			Table A1 & Fig. 5
f_{239}	3.53266±0.00016	3.41±1.49	0.28307	8	✓			r	3?	FR			Table A1 & Fig. 5
f_{240}	6.04958±0.00020	3.39±1.78	0.16530	11							$2f_{18} + 2f_{22}$		
f_{241}	23.51672±0.00025	3.39±2.26	0.04252	21									
f_{242}	3.00995±0.00015	3.35±1.35	0.33223	7	✓			g	-2?	FR	$2f_{16} - f_{43}$		Table 3 & Fig. 5
f_{243}	13.96989±0.00024	3.32±2.09	0.07158	14									
f_{244}	4.03601±0.00017	3.31±1.47	0.24777	8									
f_{245}	3.39771±0.00016	3.30±1.41	0.29432	7	✓			r	3?	FR			Table A1 & Fig. 5
f_{246}	3.19086±0.00016	3.15±1.35	0.31340	7	✓			g	-2?	FR			Table 3 & Fig. 5
f_{247}	4.16959±0.00018	3.01±1.41	0.23983	7									
f_{248}	13.97509±0.00027	3.00±2.13	0.07156	14									

Table A2. continued.

Table A2. continued.

f_i	$f \pm \epsilon_f$ d^{-1}	$A \pm \epsilon_A$ μmag	Π d	SNR	P	PS	FS	mode	m	FR/SR	comb.	MC	ref.
f_{291}	7.71673±0.00028	1.92±1.41	0.12959	7									
f_{292}	16.07896±0.00034	1.84±1.68	0.06219	10									
f_{293}	6.27130±0.00023	1.83±1.13	0.15946	6									
f_{294}	13.98038±0.00033	1.83±1.61	0.07153	8									
f_{295}	6.42793±0.00023	1.82±1.14	0.15557	6									
f_{296}	22.88613±0.00038	1.80±1.83	0.04369	12									
f_{297}	15.90034±0.00036	1.77±1.68	0.06289	10									
f_{298}	13.21455±0.00035	1.76±1.63	0.07567	9									
f_{299}	7.65563±0.00026	1.75±1.21	0.13062	6		✓		<i>p</i>		SR			Table 2 & Fig. 3
f_{300}	15.05330±0.00034	1.67±1.51	0.06643	8									
f_{301}	7.24786±0.00026	1.63±1.11	0.13797	5		✓		<i>p</i>		SR			Table 2 & Fig. 3
f_{302}	9.67081±0.00032	1.62±1.38	0.10340	7									
f_{303}	11.95624±0.00030	1.60±1.27	0.08364	7		✓		<i>p</i>		FR	$f_1 - f_{16}$	✓	Table 2 & Fig. 3
f_{304}	8.10046±0.00027	1.56±1.11	0.12345	5		✓		<i>p</i>		SR			Table 2 & Fig. 3
f_{305}	19.38475±0.00039	1.55±1.61	0.05159	8		✓		<i>p</i>		FR			Table 2 & Fig. 3
f_{306}	23.41349±0.00040	1.54±1.63	0.04271	9									
f_{307}	17.73719±0.00037	1.52±1.51	0.05638	8									
f_{308}	9.81926±0.00030	1.51±1.21	0.10184	6		✓		<i>p</i>		SR			Table 2 & Fig. 3
f_{309}	15.02743±0.00038	1.45±1.46	0.06654	8									
f_{310}	15.51649±0.00037	1.42±1.41	0.06445	7									
f_{311}	19.48475±0.00037	1.42±1.42	0.05132	7		✓		<i>p</i>		FR			Table 2 & Fig. 3
f_{312}	15.94256±0.00039	1.41±1.47	0.06273	8									
f_{313}	13.82395±0.00037	1.40±1.39	0.07234	7									
f_{314}	10.43538±0.00030	1.37±1.11	0.09583	5									
f_{315}	17.73245±0.00041	1.35±1.47	0.05639	8									
f_{316}	15.88875±0.00040	1.33±1.41	0.06294	7									
f_{317}	16.07328±0.00038	1.33±1.35	0.06222	7									
f_{318}	20.92450±0.00046	1.32±1.62	0.04779	8									
f_{319}	15.19383±0.00038	1.31±1.34	0.06582	7									
f_{320}	13.58882±0.00036	1.27±1.21	0.07359	6		✓		<i>p</i>		FR			Table 2 & Fig. 3
f_{321}	13.96839±0.00033	1.27±1.12	0.07159	5									
f_{322}	15.02920±0.00033	1.27±1.12	0.06654	6									
f_{323}	15.37967±0.00035	1.20±1.13	0.06502	6									
f_{324}	17.92462±0.00039	1.20±1.26	0.05579	7									
f_{325}	19.84820±0.00043	1.20±1.37	0.05038	7									
f_{326}	19.35654±0.00036	1.16±1.11	0.05166	5		✓		<i>p</i>		SR			Table 2 & Fig. 3
f_{327}	22.16604±0.00043	1.11±1.27	0.04511	7									
f_{328}	20.23708±0.00039	1.09±1.13	0.04941	6									
f_{329}	20.92620±0.00039	1.09±1.14	0.04779	6									
f_{330}	23.13821±0.00044	1.04±1.21	0.04322	6									
f_{331}	23.13300±0.00041	1.03±1.12	0.04323	6									